Heterogeneity-induced mixing and reaction hotspots facilitate Karst propagation in coastal aquifers

K.De Vriendt[1,2], M.Pool[1,3], M.Dentz[1]

[1]Institute of Environmental Assessment and Water Research, IDAEA-CSIC, 08034 Barcelona, Spain
[2]Department of Civil and Environmental Engineering, Technical University of Catalonia (UPC), 08034 Barcelona, Spain
[3]AMPHOS 21 Consulting S. L., 08019 Barcelona

Key Points:

- Heterogeneity results in localized reactive hotspots across the entire mixing zone.
- The presence of heterogeneity may provide an explanation for complex dissolution features observed in coastal karstic systems.

Corresponding author: Marco Dentz, marco.dentz@csic.es

Abstract

The freshwater seawater mixing zone is a critical region for chemical activity. Yet, little is known about the influence of ever present spatial heterogeneity on the dynamics of mixing and calcite dissolution, which play a key role in the understanding of Karst development. We analyse the impact of different heterogeneity structures and strengths on the local and global response of mixing and dissolution rates across the saltwater freshwater mixing zone. We find that the initial heterogeneity structure significantly impacts on observed dissolution and mixing patterns, which sheds some new light on Karst propagation in coastal aquifers.

1 Introduction

The mixing of freshwater and seawater in coastal carbonate formations has been long associated with zones of high porosity development and elaborate cave networks [*Back et al.*, 1986]. The presence of caves in the Yucatan peninsula [*Back et al.*, 1979, 1986; *R.K. Stoessell, W.C. Ward, B.H. Ford*, 1989] and enhanced porosity observed from cores collected in the Bermudas Andros island [*Smart et al.*, 1988] for example, have been directly attributed to mixing dynamics across the salt-freshwater mixing zone. Despite this, limited accessibility to deeper portions of the mixing zone has prevented large scale surveys of caves which may otherwise be available further inland. Since the topology of many karstic networks and their subsequent geomorphological characteristics are strongly linked to their flow regimes and local geology [*Jouves et al.*, 2017], understanding the behaviour of mixing and reactions under variable density flow in coastal systems under the influence of various types of heterogeneity may offer insight into the localisation of preferential calcite dissolution, which may be particularly important during the initial stages of karst propagation.

Numerical studies have previously demonstrated that calcite dissolution at the seawater-freshwater interface occurs dominantly across the fresher spectrum of the mixing zone where mixing waters are most strongly undersaturated with respect to calcite [*Sanford and Konikow*, 1989; *Rezaei et al.*, 2005]. Moreover, *Sanford and Konikow* [1989] found that dissolution takes place in fresher water then what would be expected by simple mixing alone. Interestingly, two reactive hotspots were also observed; one in fresher portion of the mixing zone at the toe and one in saltier portion of mixing waters at the discharge zone. These behaviours have been attributed to an initial mixing effect at the toe, which gives way to the highest potential for undersaturation and enhanced dispersive mixing at the discharge zone. While these homogeneous studies have provided valuable insight into the interplay between transport and chemical reactions, they fall short of explaining the maze-like conduit networks observed in real karst aquifers.

Coastal carbonate aquifers present heterogeneous discontinuities, such as fractures, dikes, and large scale stratification, which may induce complex salinity distributions leading to irregular patterns of enhanced local mixing and reactive hotspots, this means zones of enhanced reactivity. It is well known that heterogeneity of hydraulic properties strongly controls solute spreading and mixing in porous media [*Dagan*, 1987; *Gelhar*, 1993, 2003; *Dentz et al.*, 2011]. Heterogeneity has also been suggested as an important mechanism toward realistic representations of offshore submarine groundwater discharge [*Michael et al.*, 2016]. However, only few studies have addressed heterogeneity for variable density flow systems and, in particular, for seawater intrusion problems [see, e.g., *Held, R, S.Attinger*, 2005; *Abarca*, 2006; *Kerrou and Renard*, 2010; *Sebben et al.*, 2015; *Pool et al.*, 2015]. In general, it has been found that heterogeneity leads to increased spreading of the freshwater-seawater mixing zone. While it is evident that heterogeneity plays a strong role in mixing in many subsurface groundwater problems, its impact on mixing-limited reactions such as calcite dissolution in coastal variable density flow systems remains an open question.

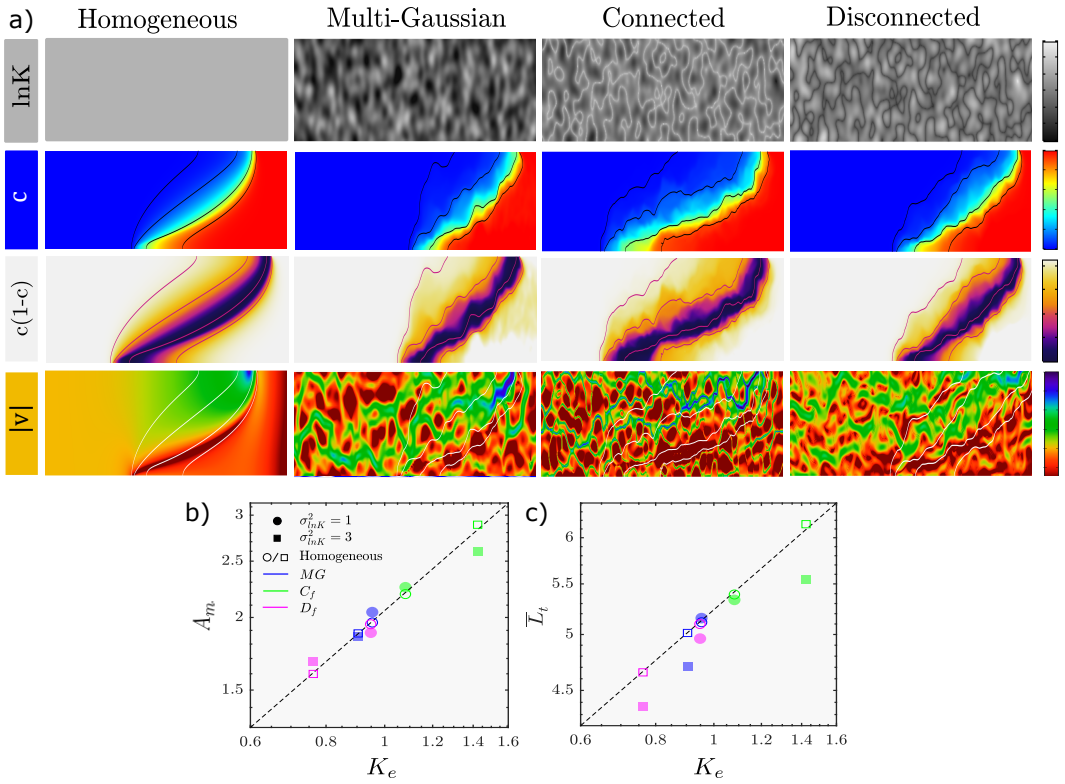

Figure 1. Maps showing examples of (from top to bottom) the hydraulic conductivity field for the homogeneous and heterogeneous fields ($\sigma^2_{lnK} = 1$), the mixing ratio (c), $c(1-c)$ and the logarithm of the velocity modulus ($|v|$). b) The non-dimensional average mixing area ($\overline{A}_m$) and c) the toe position ($\overline{L}_t$) against their non-dimensional hydraulic conductivity (K_e). The dashed lines denote the dependence of the mixing area and toe position on hydraulic conductivity for an equivalent homogeneous medium. Mixing ratio contours displayed in the maps correspond to mixing ratios of 1%, 10%, 50% and 95%.

.

In this paper we investigate the effect of heterogeneity and connectivity on mixing and chemical reactions across the salt-freshwater interface under steady-state conditions. We consider a fast calcite dissolution reaction to explore karstification processes induced by mixing in coastal aquifers. Two-dimensional variable density flow and transport simulations are performed considering large scale hydraulic conductivity stratification and log-normally distributed mulit-Gaussian hydraulic conductivity fields. In addition, more complex heterogeneous fields characterized by connected and disconnected patterns of high and low conductivity are considered. We analyze the mixing and reaction dynamics by focusing on the local and global reaction and mixing rates. Our results aim to provide insight into the role of heterogeneity in non-uniform flow fields such as that induced by seawater intrusion in an effort to provide more realistic representation of mixing and calcite dissolution that may act as precursors to the propagation and creation of complex karst networks in coastal environments.

2 Methods

We study mixing and calcite dissolution patterns under steady variable density flow in two-dimensional heterogeneous coastal aquifers. Density-dependent flow is described

by the Darcy equation

$$\mathbf{q}(\mathbf{x}) = -K(\mathbf{x}) \left[\nabla h_f(\mathbf{x}) + \frac{\rho(\mathbf{x}) - \rho_f}{\rho_f} \mathbf{e}_z \right], \tag{1}$$

where $\mathbf{x} = (x, z)^\top$ is the coordinate vector, $\mathbf{q}(\mathbf{x})$ the specific discharge, $K(\mathbf{x})$ hydraulic conductivity, $h_f(\mathbf{x})$ the equivalent freshwater head, $\rho(\mathbf{x})$ the fluid density, ρ_f the density of freshwater and $\mathbf{e}_z$ is the unit vector in z-direction. Fluid mass conservation in the absence of sources and sinks implies $\nabla \cdot \rho(\mathbf{x})\mathbf{q}(\mathbf{x}) = 0$. The fluid density depends on the mixing ratio $c(\mathbf{x})$ between fresh and seawater and is assumed to be linearly dependent on the salt mass fraction $\omega(\mathbf{x})$ (mass of salt dissolved per unit mass of fluid) given by $\rho(\mathbf{x}) = \rho_f[1 + \beta c(\mathbf{x}, t)]$ where β is the buoyancy factor given by $\beta = (\rho_s - \rho_f)/\rho_f$ and ρ_s is the density of seawater. The mixing ratio is given by $c(\mathbf{x}) = \omega(\mathbf{x})/\omega_s$ with $\omega(\mathbf{x})$ the salt mass fraction in the mixture and ω_s the salt mass fraction of seawater. Thus, it obeys the steady state advection-dispersion equation [*Voss and Provost*, 2002],

$$\mathbf{q}(\mathbf{x}) \cdot \nabla c(\mathbf{x}) - \nabla \cdot [\mathbf{D}(\mathbf{x}) + \phi D_m] \nabla c(\mathbf{x}) = 0, \tag{2}$$

with $\mathbf{D}(\mathbf{x})$ the dispersion tensor [*Bear*, 1988], D_m molecular diffusion and ϕ porosity.

The flow domain is 1500 m long and 100 m wide with a prescribed freshwater flux of 250 m/a and zero mixing ratio at the inland boundary at $x = 0$ and hydrostatic saltwater at the seaward boundary. The mixing ratio and the inland boundary is set to 0, while the mass flux at the seaward boundary is set equal to the advective flux of seawater if the horizontal component of $\mathbf{q}$ point inland and equal to the advective flux of the local mixing ratio otherwise. A detailed relation of the numerical setup can be found in section 3 of the supporting information. Hydraulic conductivity $K(\mathbf{x})$ is modelled as a two dimensional spatial random field. We consider multi-Gaussian (MG), as well fields of connected high (C_f) and low hydraulic conductivity (D_f). All fields are characterized by log-normal point statistics with variances of the log-hydraulic conductivity $\sigma^2_{lnK} =$ 1 and 3. The connected high (C_f) and low hydraulic conductivity (D_f) serve to mimic the presence of channels or fractures.

In order to highlight the influence of heterogeneity on mixing and reaction efficiency, we compare the results from the heterogeneous to equivalent homogeneous scenarios. For each type of heterogeneity and log-K variance, 10 equally probable realizations are considered. The observables presented in the following are obtained by averaging over the set of realizations for each heterogeneity type (averaged quantities are denoted by an overline). While we consider only a limited number of realizations due to computational constraints, the variability between realizations is low such that the average can be considered representative for the heterogeneity impact on the mixing and reaction behaviour. Furthermore, in order to illustrate reactive patterns that may emerge in the presence of large scale discontinuities, we consider in Section 3.3 two realizations of a stratified multi-Gaussian aquifer structure characterized by infinite longitudinal correlation length, transverse correlation length of 10 m and $\sigma^2_{lnK} = 1$ and 3. Details are given in Section 4 of the supporting information.

Figure 1a illustrates maps of the mixing ratio and velocity magnitude for homogeneous, multi-Gaussian, connected and disconnected hydraulic conductivity fields. The mixing area $\overline{A}_m$ between fresh and seawater shown in Figure 1b is defined as the area comprised between the 0.95 and 0.01 isolines of the mixing ratio. The penetration depth $\overline{L}_t$ of the seawater wedge shown in Figure 1c is defined as the distance of the 0.5 isoline of the mixing ratio from the seaside boundary. Note that both these quantities are averaged across all realizations. The mixing area and penetration depth are non-dimensionalized in terms of the characteristic length scale l_c, which here is identified with the height of the domain.

In order to investigate the influence of heterogeneity on mixing and reaction efficiency, we compare the results from the heterogeneous realizations to equivalent homo-

geneous media. In order to determine the effective hydraulic conductivity of the equivalent media, a constant hydraulic head gradient is imposed between the inland and the seaside boundaries for each heterogeneous realization, with the horizontal boundaries defined as no flow boundaries. The effective hydraulic conductivity K_e is given by the ratio between the total flow rate across the seaside boundary and the average hydraulic head gradient. The effective hydraulic conductivity is nondimensionalized by the geometric mean conductivity K_g, which for all fields under consideration is $K_g = 5{\cdot}10^{-4}$ m/s. Note that for isotropic multi-Gaussian fields, K_g is equal to the effective conductivity [see, e.g. *Renard and de Marsily*, 1997; *Sanchez-Vila et al.*, 2006]. As evidenced in Figure 1 (b-c), $\overline{K}_e$ corresponds well to the level of connectivity of each field. As found by *Zinn and Harvey* [2003], connectivity results in an increase in $\overline{K}_e$. Furthermore, as observed for multi-Gaussian heterogeneous media [*Abarca*, 2006; *Kerrou and Renard*, 2010], we see in Figure 1 (b-c) that both $\overline{L}_t$ and $\overline{A}_m$ decrease with increasing heterogeneity This can be directly linked to a decrease in $\overline{K}_e$. For the connected fields $\overline{K}_e$ increases with increasing heterogeneity. In general we see that increase or decrease in $\overline{K}_e$ directly corresponds to increase or decrease in toe length and mixing area for both the homogeneous and heterogeneous fields.

The mixing and reaction behaviour and its impact on karst propagation are studied through the process of mixing-induced calcite dissolution. In the considered setting, we use the two representative end-members of freshwater and seawater according to *Rezaei et al.* [2005]. The seawater composition represents water collected from boreholes in a coastal aquifer from Grand Cayman [*Ng and Jones*, 1995] while the freshwater compositions represents distilled water in equilibrium with calcite, see Table 1 in the supporting information for the details of the chemical system. When the respective equilibria are perturbed due to mixing, the new chemical equilibrium of the mixture is established instantaneously. This is a reasonable assumption for coastal aquifers where calcite dissolution is fast relative to the residence times of water [*Sanford and Konikow*, 1989; *Rezaei et al.*, 2005]. We consider the chemical system detailed in *De Simoni et al.* [2007] under conditions that lead to undersaturation upon mixing and thus calcite dissolution. Note that this study does not incorporate any feedback between chemical reactions and the flow and transport properties. The equilibrium reaction rate can then be written in the form

$$r(\mathbf{x}) = \Lambda(\mathbf{x})\chi(\mathbf{x}), \tag{3}$$

where $\chi(\mathbf{x})$ is the local mixing rate,

$$\chi(\mathbf{x}) = \nabla c(\mathbf{x}) \cdot [\mathbf{D}(\mathbf{x}) + \phi D_m] \nabla c(\mathbf{x}). \tag{4}$$

Reaction and mixing rates are non-dimensionalized in the following according to $r' = rl_c/q_f\sqrt{K_{eq}}$, and $\chi' = \chi l_c^2/\alpha_g q_f$ where α_g is the geometric mean of the longitudinal and transverse dispersivities, q_f is the inland freshwater flux, K_{eq} is the solubility product for calcite dissolution. In the following, we omit the primes for simplicity of notation. The mixing rate χ measures the dynamics of conservative mixing between fresh and saltwater. The chemistry is contained in the speciation intensity Λ as outlined in detail in Section 2 of the Supporting Information. Note that the term equilibrium reaction rate may appear contradictory. However, it describes the rate of reaction due to fast chemical equilibration of two endmembers upon mixing. Therefore it is dominated by the mixing rate χ, whose magnitude depends on both concentration gradients and dispersion coefficients. In our analysis we assess the average scalar dissipation rate $\langle\chi\rangle$ and reaction rate $\langle r\rangle$ per unit mixing area. This facilitates the intercomparison of heterogeneous fields with respect to the corresponding homogeneous scenarios.

3 Results and Discussion

We discuss here the impact of heterogeneity on mixing and dissolution patterns and their subsequent implications on the propagation of karsts.

3.1 Influence of Heterogeneity on Mixing Rate

Figure 2 shows the strong impact that the presence of heterogeneity has on both the mixing and reaction rate across the interface. At the top of the transition zone, high velocities induced by the freshwater discharge translate to strong dispersive mixing [*Rezaei et al.*, 2005]. This is reflected in χ for both the homogeneous and heterogeneous media. It can be observed that heterogeneity-induced velocity variations lead to both greater variability, and the steepening of concentration gradients resulting in enhanced mixing along the mixing interface. As expected, since χ depends on both the presence of concentration gradients and dispersion, the largest values are localized in high-K zones, where velocities and thus dispersion are large. Note that while χ is generally highest along the 50% mixing ratio contour, near the toe it extends into the fresher portion of the mixing zone. This can be likely attributed to enhanced interface compression that accompanies stagnation points [see, e.g., *Ranz*, 1979; *Hidalgo and Dentz*, 2018], which for the seawater intrusion problem, exists at the toe. This observation suggests that the localised hotspot at the toe it not simply the result of the previously mentioned initial-mixing effect [*Sanford and Konikow*, 1989; *Rezaei et al.*, 2005], but also due to strong flow deformation.

As shown in Figure 2c, $\langle\chi\rangle$ decreases linearly with increasing effective hydraulic conductivity for homogeneous media. There are two factors dominating $\langle\chi\rangle$. We first observe that the presence of hetereogeneity in general and the value of logK variance in particular result in an increase of $\langle\chi\rangle$ for all fields with respect to their homogeneous equivalent. This is most notable for the connected scenarios, for which the mixing rate increases up to a factor of 2. Additionally, we see that K_e strongly controls the behaviour of $\langle\chi\rangle$ for homogeneous and weakly heterogeneous fields. This may be understood as follows. For high K_e, the interface penetrates further and is flatter than for low K_e. Thus, at high K_e, there is a lower velocity contrasts between the flowing freshwater body and the convection cell at the seaside boundary. Reduction of velocity contrast leads to a reduction of concentration contrast, which in turn reduces the mixing rate.

3.2 Influence of Heterogeneity on the Reaction rate

In accordance with the studies of *Sanford and Konikow* [1989] and *Rezaei et al.* [2005], zones of enhanced calcite dissolution are shown to occur near the fresher spectrum of the mixing zone see Figure 2a. This is once again due to the fact that the speciation intensity, which is a non-linear function of the mixing ratio, concentrates at the freshwater dominated part of the mixing zone. In fact, reaction hotspots may be due to a high local speciation intensity in a moderate mixing background, or due to a high mixing rate in a background of moderate speciation intensity. For the homogeneous scenarios, as expected, one observes two significant reaction hotspots at the top and bottom of the mixing zone. The reaction hotspot at the top of the aquifer coincides with the mixing hotspot, while the reaction hotspot at the toe is determined by high speciation intensity in the presence of moderate mixing. Our simulations reveal that heterogeneity induces highly irregular distributions of reaction rates that strongly deviate from the homogeneous case.

This is further evidenced in Figure 2b, which shows the vertically integrated heterogeneous reaction rate profiles compared to their respective effective homogeneous behaviour. In the presence of heterogeneity, distinct reaction hotspots emerge along the interface whose density and intensity increase with increasing heterogeneity and also with the connectivity. Thus, spatial heterogeneity broadens the spectrum of local reaction rates towards high values compared to homogeneous media. In Figure 2d, we observe that, for the exception of the high variance connected field, $\langle r\rangle$ is smaller for heterogeneous fields compared to the respective homogeneous case. This can be understood by the increased segregation of high-K zones, where reactions preferentially occur. In the case of the high variance connected field, an increase in $\langle r\rangle$ compared to the homogeneous sce-

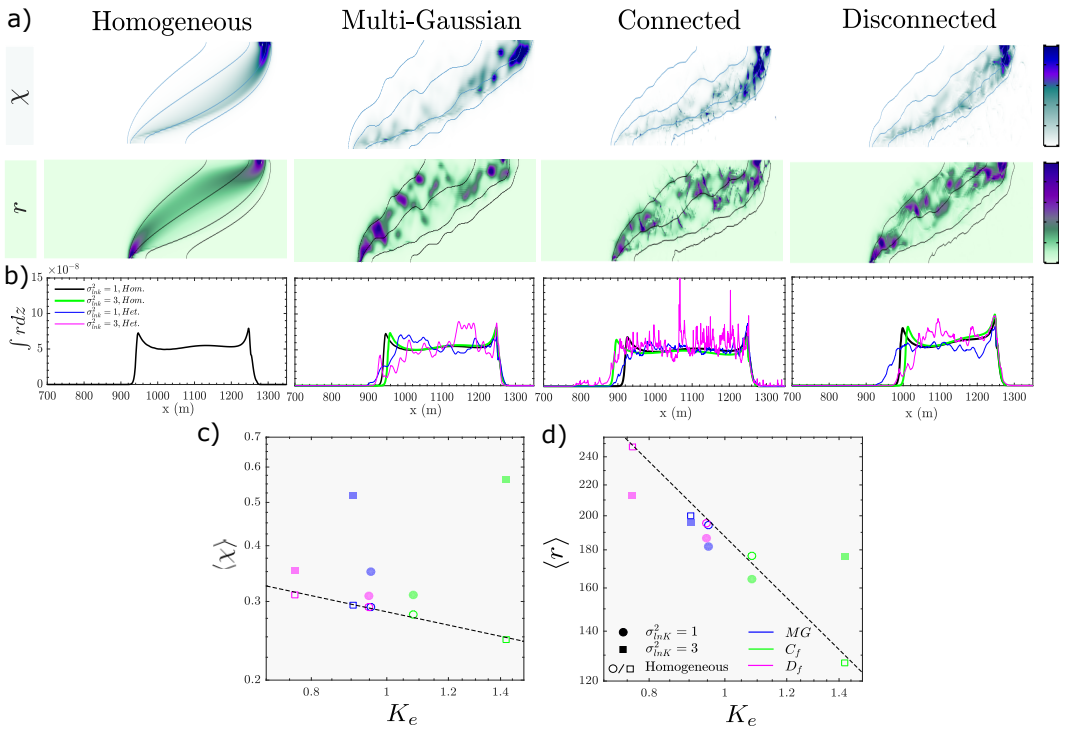

Figure 2. Examples of maps for ($\sigma^2_{lnK} = 3$) corresponding to (from top to bottom) the average mixing and reaction rates and the vertically integrated reaction rate for the homogeneous, multi-Gaussian (MG), connected (C_f) and disconnected fields (D_f). The scatter plot at the bottom shows the average non-dimensional mixing rate ($\langle\chi\rangle$) and non-dimensional reaction rates ($\langle r\rangle$) for their corresponding non-dimensional effective hydraulic conductivities $\overline{K}_e$. Mixing ratio contours displayed in the maps correspond to mixing ratios of 1%, 10%, 50% and 95%. The dashed lines denote the dependence of the mixing and reaction rate on hydraulic conductivity for an equivalent homogeneous medium

nario can be attributed to the strongly enhanced mixing rates observed in Figure 2c, which permits reactions to occur over a larger portion of the mixing zone.

While the spatial variability of reactions are strongly impacted by the presence of heterogeneity, we see that, similar to the behaviour of $\langle\chi\rangle$ for homogeneous and weakly heterogeneous scenarios, $\overline{K}_e$ exerts a strong control over $\langle r\rangle$, even for the higher log-K variance disconnected and multi-Gaussian fields. It should be reiterated that while an increase in $\overline{K}_e$ lengthens the interface, which increases the area over which mass-transfer can occur, the velocity and concentration contrasts at the mixing interface are higher when the toe is closer to the seaside boundary, resulting in higher averaged reaction rates per unit area.

3.3 Influence of Heterogeneity on Reactive Patterns

The type of imposed heterogeneity manifests in particular patterns of enhanced reactivity in the presence of the non-uniform flow field. Multi-Gaussian fields for example, are characterized by hotspots that radiate concentrically, while connected field hotspots are predominantly isolated in high-K channels that are orientated vertically, parallel to the local direction of flow. For the disconnected field, reaction patterns are qualitatively

similar to multi-Gaussian fields, but they also contain zones of enhanced reaction that straddle low-K channels, perpendicular to the local direction of flow, asa can be seen in Figure 3. It is interesting to note that despite the apparent connectivity of the imposed heterogeneous structures, zones of enhanced reactivity tend to emerge as unconnected features. This suggests that during early stages of diagenesis, the spatial location and orientation of hydraulic features during seawater intrusion may strongly control the transient evolution of caves.

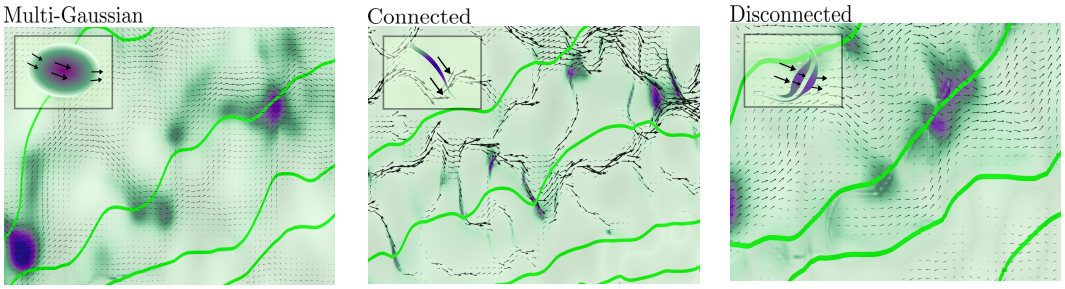

Figure 3. Zoomed in sections of the Reaction field overlaid with their corresponding hydraulic conductivity field. Arrows represent flow directions whose length is proportional to the logarithm of velocity.

Simulations of seawater intrusion in horizontally stratified hydraulic conductivity provides further insight to calcite dissolution in the presence of large scale connectivity. We observe that vertical changes in hydraulic conductivity causes strong veloctity and concentration contrast across the mixing interface which manifests as narrow, elongated zones of enhanced reactivity. In Figure 4, we see that by increasing the log-K variance, strong concentration contrast along the low-K layers lead to enhanced reactions. In addition to the stratified multi-Gaussian fields, simulations for discrete low-high-low (1:10:1) and high-low-high (10:1:10), further isolates these dynamics. We see that when a low-conductive material sandwiches a high-conductive layer, strong dissolution occurs at the base of the high-K zone, whereas strongest dissolution is observed at the top of the stratified layer for the high-low-high K scenario. This illustrates that reaction is enhanced when flow is directed from a low to high-K medium, which sheds light on the preferential development of karstic systems.

4 Concluding remarks

The topology of karst conduits have been strongly linked to their spatial location and the governing flow characteristics [e.g., *Palmer*, 1992; *Audra and Palmer*, 2015; *Gabrov et al.*, 2014]. For example, anastomosic caves, defined by their braided patterns, typically occur across bedding planes in the epiphreatic zone, whereas angular mazes tend to be associated with fractured media due to seepage from overlying insoluble rocks [*Jouves et al.*, 2017]. While near-surface features such as flank margin caves [*Mylroie and Carew*, 1990] can be observed in many coastal carbonate environments along the salt-freshwater mixing zone, limited accessibility has prevented large-scale speleological surveys of karst conduits in coastal aquifer. Consequently, no formal characteristics exist to describe dissolution patterns at depth across the mixing zone. It is therefore possible, that many hydraulically dominant karstic features may exist outside our current ability to observe.

Our study suggests that the initial stages of karst development, also known as the laminar flow phase [*Lowe*, 1992], may be a crucial period which influences the subsequent evolution of a karstic conduit. The importance of early-stage karst development was also investigated by *Groves and Howard* [1994], who found that enlargement of conduits in

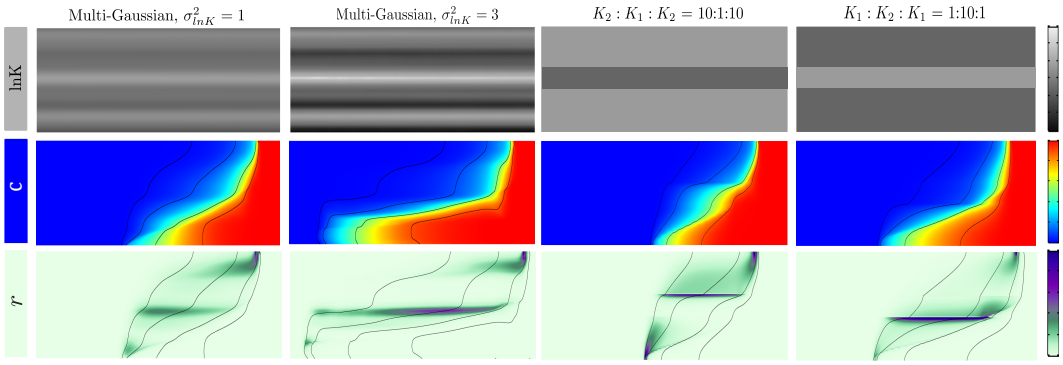

Figure 4. Horizontally stratified hydraulic conductivity fields. From top to bottom are the log-K, the mixing-ratio, and reaction rate fields. The two left-most columns show the results for the multi-Gaussian stratified scenario for $\sigma^2_{lnK} = 1$ and 3 while the two right-most columns show the results for an aquifer whose hydraulic conductivity is discretely layered. The third column shows the results for a K-ratio of 10:1:10 while the fourth column shows the result for a K-ratio of 1:10:1.

coastal carbonate aquifers occurs very selectively during the laminar flow regime. Geomorphological studies on phreatic karstic caves have shown that over 70% of conduits develop along discrete bedding planes in limestones [*Filipponi et al.*, 2009], known as 'inception horizons' [*Lowe*, 1992]. Such features are the result of physical, lithological and chemical deviations from the central carbonate facies. Cave surveys have shown that inception horizons may play a strong role during the most early stages of karst formation [*Filipponi et al.*, 2009]. In the simplest case of large scale horizontal stratification, our study suggests that in coastal environments, due to the density-driven convection and subsequent upward re-circulation of flow, even simple changes in hydraulic conductivity could be very sensitive to enhanced dissolution. *Sanford and Konikow* [1989] showed that a migrating seawater wedge in a homogeneous media results in increased permeability which would consequently shift the wedge further inland. One could therefore imagine that large-scale sea level and tidal fluctuations could generate elongate karstic features that extend many kilometres inland.

It should be noted that, while karstification is inherently a 3D process, our study sheds light on the fundamental mechanisms relating medium structure, flow heterogeneity, and mixing and dissolution. Due to their fundamental nature, we expect them to be qualitatively similar in 3D. This refers particularly to the finding that the initial structure of the aquifer and its impact over the mixing and reaction patterns plays a key role for understanding the development of realistic karstic systems observed across modern coastlines.

Acknowledgments
Data associated with this manuscript are available in the DIGITAL.CSIC repository at https://digital.csic.es/ under the DOI: http://dx.doi.org/10.20350/digitalCSIC/8955.
This project has received funding from the European Union's Horizon 2020 research and innovation program under the Marie Sklodowska-Curie Grant Agreement No. 722028 (ENIGMA ITN).

A: Chemical system

We consider the two end-member chemical composition specified by *Rezaei et al.* [2005]. In order to attain the local reactions rates across the salt freshwater interface we employ a mixing-ratio based method for reactive transport. Since this method decouples the solute transport and chemical speciation components of the problem, the mixing ratios must first be found by solving the conservative transport problem. The concentrations of the reacting species can then be found using a general speciation code. In this work, PHREEQC was employed. In order to calculate the concentrations of our reacting species, PHREEQC is provided with the chemical compositions of the fresh and saline groundwater. For this we use the end-member compositions given in the table provided below (see Table A.1). PHREEQC performs the speciation calculations for a given set of mixing ratios ranging between 0 an 1. From here we can now plot the second derivative of our secondary species (Ca^{2+}) with respect to the mixing ratio ($\delta^2 Ca^{2+}/\delta^2\alpha$) against our range of mixing ratios which will be used to solve the local reaction rates across the mixing zone (see Figure A.1).

Table A.1. Chemical composition of end-members used in speciation calculations. All concentration units are in $mmol \cdot kg^{-1}$

Solution	**pH**	**Ca**	**Mg**	**Na**	**K**	**Cl**	**log** P_{CO_2}	I
Seawater	7.21	9.64	22.43	496.53	9.28	564.13	-2.01	6.25
Freshwater	7.30	1.65	0.00	0.00	0.00	0.00	-2.00	0.005

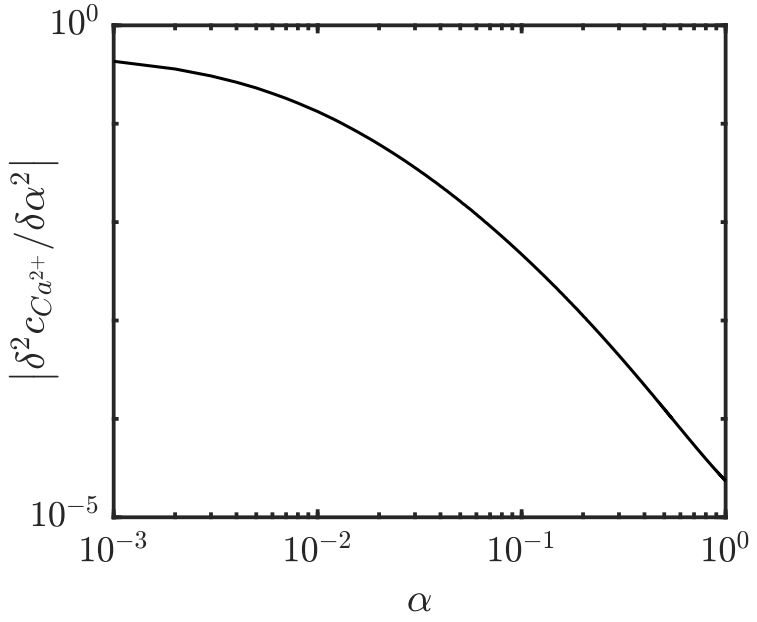

Figure A.1. Dependence of the absolute of $\delta^2 Ca^{2+}/\delta^2\alpha$ on α

B: Numerical flow and transport model

B.1 Field generation

We generate multi-Gaussian (MG) random fields with a geometric mean of $5{\cdot}10^{-4}$ m/s and log-conductivity variances of $\sigma^2_{\ln k}$=1 and 3 using a discrete fourier transform technique (e.g. Cirpka and Kitandis, 2002). The Multi-Gaussian fields are characterized by an Gaussian covariance function with isotropic correlation length of 10 m. From the respective MG fields, fields of connected high and low values are obtained following the method of *Zinn and Harvey* [2003].

B.2 Variable density flow and transport

Fluid-density-dependent saturated flow and transport simulations were performed with COMSOL Multiphysics®. The governing equations for variable density flow and transport are described by the Darcy law and the steady state advection-dispersion equation, see Equations 1 and 2 in the main paper. Note that while it is common to use a transverse to longitudinal dispersivity ratio of 0.1, we choose a ratio of 0.5 which has also been observed in seawater intrusion experiments (e.g. **??**). The model set-up is similar to that of *Sanford and Konikow* [1989] and *Rezaei et al.* [2005] with a model extent of L_x=1500m and a constant thickness of L_z =100m. The shoreline was established at x = 1250 m. The model was discretized into 2×2 m^2 regular cells. The discretization satisfies the mesh peclet number criterion [**?**] such that

$$Pe_m = \frac{q_f \Delta L}{D_m + \alpha_L q_f} \leq 4, \tag{B.1}$$

where ΔL is the grid size. This criterion ensures oscillations in the concentration distribution are minimized. The mixing ratio is defined by the normalized salt mass fraction $c = \omega/\omega_s$ with ω the salt mass fraction of the fluid and ω_s the seawater salt mass fraction. The boundary conditions adopted consist of a prescribed constant freshwater flow rate of q_f at the inland boundaries and prescribed hydrostatic pressure along the offshore boundaries as shown in Figure B.1. The mixing ratio at the vertical inland boundary is given by the Dirichlet condition $c(\mathbf{x}) = 0$ at $x = 0$, and at the vertical offshore boundary by the Neumann boundary condition $\frac{\partial c(\mathbf{x})}{\partial x} = 0$ at $x = L_x$. The latter implies that water with $c = 1$ enters the aquifer at the locations at which $q_x < 0$ and water with the formation mixing ratio c exits where $q_x > 0$. The bottom boundary is a no-flow boundary for both salt mass fraction and water. The numerical values of the modeling parameters are provided in Table B.1. A schematic of the modeling domain and the applied boundary conditions is shown in Figure B.1. Models were run until the steady state for both heads and concentrations was reached. An adaptive timestepping scheme is used which automatically adjusts the time step in order to maintain the desired relative tolerance. We consider for each heterogeneity setup 10 equally probable realizations.

C: Observables

The observables are obtained by ensemble averaging over the realizations for each heterogeneity type. While we consider only a limited number of realizations due to computational constraints, the variability between realizations is low such that the average can be considered representative for the heterogeneity impact on the mixing and reaction behavior.

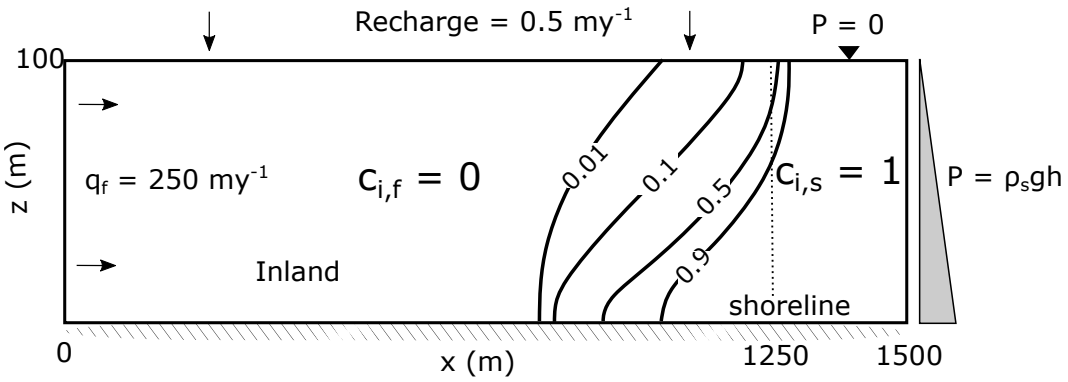

Figure B.1. Boundary conditions and initial conditions for the of the given saline intrusion problem.

Table B.1. Summary of key parameters values used in the numerical simulations

Parameter	Description	Value	Unit
K_G	Geometric mean conductivity	5e-4	ms^{-1}
q_f	Inland freshwater flux	250	myr^{-1}
ϕ	Porosity	0.3	-
α_L	Longitudinal dispersion	6	m
α_T	Transverse dispersion	3	m
R	Recharge	0.5	$my^{-}1$
ρ_f	Freshwater density	1.00e3	kgm^{-3}
ρ_s	Seawater density	1.025e3	kgm^{-3}
ρ_s	Fluid viscosity	1.00e-3	kg$m^{-3}s^{-1}$

C.1 Effective hydraulic conductivity

In order to approximate the effective hydraulic conductivity for each heterogeneous realization (multi-Gaussian, connected and disconnected fields), a hydraulic head difference of Δh =5 m was imposed across the length of the domain using two constant head boundaries with the upper and bottom boundaries defined as no flow. The mean flux was then calculated across the left boundary in order to determine the effective hydraulic conductivity as

$$K_{eff} = \frac{1}{\Delta h}\frac{L_x}{L_z}\int_0^{L_z} dz q_x(L_x, z). \tag{C.1}$$

The average effective conductivity is obtained by averaging over the realizations as

$$\overline{K}_{eff} = \frac{1}{N}\sum_{i=1}^{N} K_{eff}^i \tag{C.2}$$

Figure C.1 shows the average effective conductivity for the different conductivity fields along with the error bars. The average seems to stabilize after only 10 realizations.

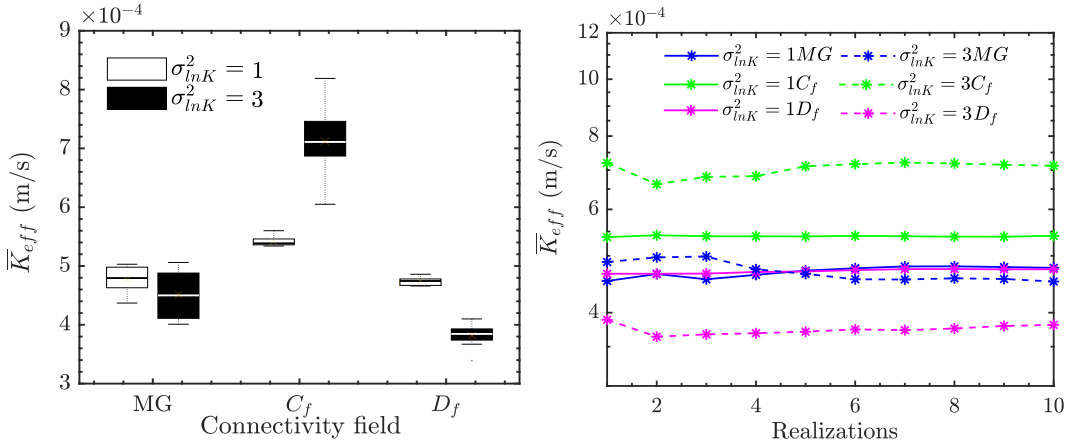

Figure C.1. Box plot (left) showing the average effective conductivity ($\overline{K}_{eff}$) for $\sigma^2_{lnK} = 1, 3$. $\overline{K}_{eff}$ is shown for each additional realisation (right).

C.2 Toe position

The toe position L_t is defined by the distance of the intersect of the $c = 0.5$ isoline with the bottom boundary and the seaward domain boundary,

$$L_t = F^{-1}(0.5), \qquad F(x) = c(x, 0) \tag{C.3}$$

The average toe position is obtain by ensemble averaging as

$$\overline{L}_t = \frac{1}{N}\sum_{i=1}^{N} L_t^i \tag{C.4}$$

Figure C.3 shows the average toe position for the different hydraulic conductivity fields.

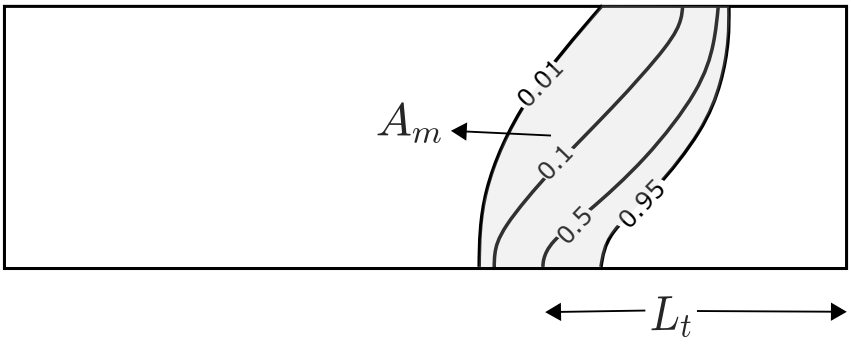

Figure C.2. Schematic showing variables of interest for saltwater mixing wedge. The diagram shows mixing ratio contour lines 0.01, 0.1, 0.5 and 0.95. The bounded shadowed area is A_m which is between mixing ratio lines 0.01 to 0.95. The arrow at the bottom of the schematic illustrates the measured length toe position (L_t).

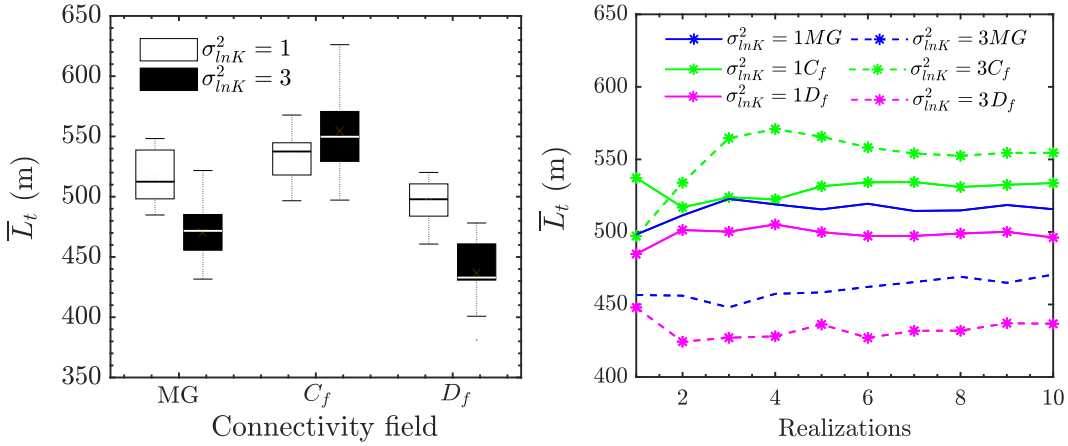

Figure C.3. Box plot (left) showing the average toe position ($\overline{L}_t$) for $\sigma^2_{lnK} = 1, 3$. $\overline{L}_t$ is shown for each additional realisation (right).

C.3 Mixing area

The Mixing Area (A_m) is defined by the area bounded between the $c_{min} = 0.01$ and $c_{max} = 0.95$ isolines of the mixing ratio,

$$A_m = \int H\left[c(x,z) - c_{min}\right] H\left[c_{max} - c(x,z)\right] dxdz \tag{C.5}$$

where H is the heaviside step function. The range was chosen in order to capture where the majority of mixing and reactions would occur. Rather than bound the mixing area by the more traditional 0.1-0.9 mixing ratio isolines we extend the dilute end to 0.01, since the fresher spectrum of mixing is important for calcite dissolution. The average mixing area is defined by

$$\overline{A}_m = \frac{1}{N} \sum_{i=1}^{N} A_m^i \tag{C.6}$$

Figure C.4 shows the average mixing area. We show that the average mixing area also stabilizes over the chosen number of realizations simulated.

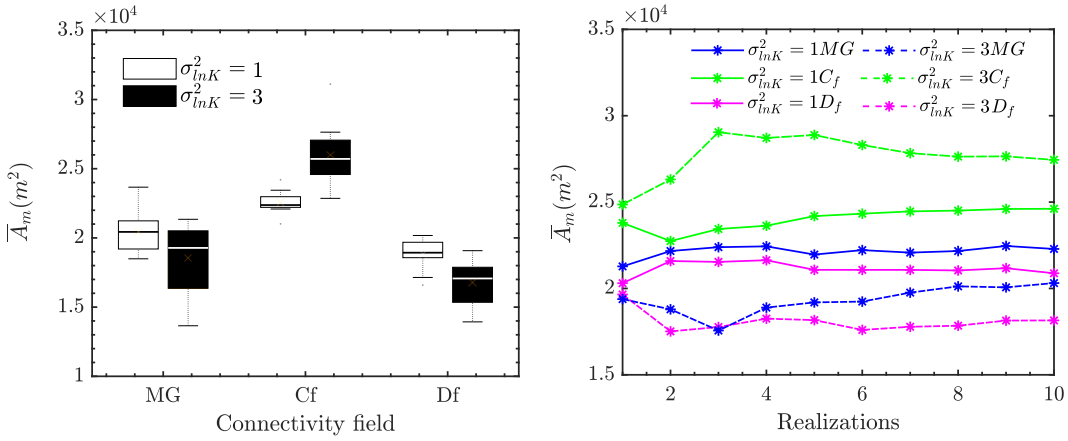

Figure C.4. Box plot (left) showing the average mixing area ($\overline{A}_m$) for $\sigma^2_{lnK} = 1, 3$. $\overline{A}_m$ is shown for each additional realisation (right).

C.4 Mixing and reaction rate statistics

The statistics of the mixing and reaction rates are sampled within the mixing zone Ω_m delimited by the $c_{min} = 0.01$ and $c_{max} = 0.95$ isolines of the mixing ratio

$$\Omega_m = \{\mathbf{x} | c_{min} < c(\mathbf{x}) < c_{max}\}. \tag{C.7}$$

Thus, the probability density function (PDF) of the mixing rate $\chi(\mathbf{x})$ is obtained by sampling the local values in each realization and constructing a normalized histogram as

$$p_\chi(\chi) = \frac{1}{N}\sum_{i=1}^{N}\frac{1}{A_m}\int_{\Omega_m} dxdz \frac{\mathbb{I}[\chi < \chi^i(\mathbf{x}) \leq \chi + \Delta\chi]}{\Delta\chi} \tag{C.8}$$

where the indicator function $\mathbb{I}(\cdot)$ is 1 is the argument is true and 0 else and $\Delta\chi$ is the bin size used to sample mixing rate data. The PDF of the reaction rates is defined in analogy as

$$p_r(r) = \frac{1}{N}\sum_{i=1}^{N}\frac{1}{A_m}\int_{\Omega_m} dxdz \frac{\mathbb{I}[r < r^i(\mathbf{x}) \leq r + \Delta r]}{\Delta r}. \tag{C.9}$$

Figure C.5 shows the PDFs of the mixing and reaction rates for the different hydraulic conductivity fields. The average mixing and reaction rates $\overline{\chi}$ and $\overline{r}$ are given by

$$\langle\chi\rangle = \int d\chi \chi p_\chi(\chi) = \frac{1}{N}\sum_{i=1}^{N}\frac{1}{A_m}\int_{\Omega_m} dxdz\chi^i(\mathbf{x}) \tag{C.10}$$

$$\langle r\rangle = \int drrp_r(r) = \frac{1}{N}\sum_{i=1}^{N}\frac{1}{A_m}\int_{\Omega_m} dxdzr^i(\mathbf{x}) \tag{C.11}$$

C.5 Horizontal Stratification

In order to provide an example for a reaction and mixing pattern that would result from horizontal stratification, we simulate seawater intrusion with a multi-Gaussian field described with an infinite longitudinal correlation length and a transverse correlation length of 10 m. This was performed for log-conductivity variances of $\sigma^2_{\ln k}$=1 and

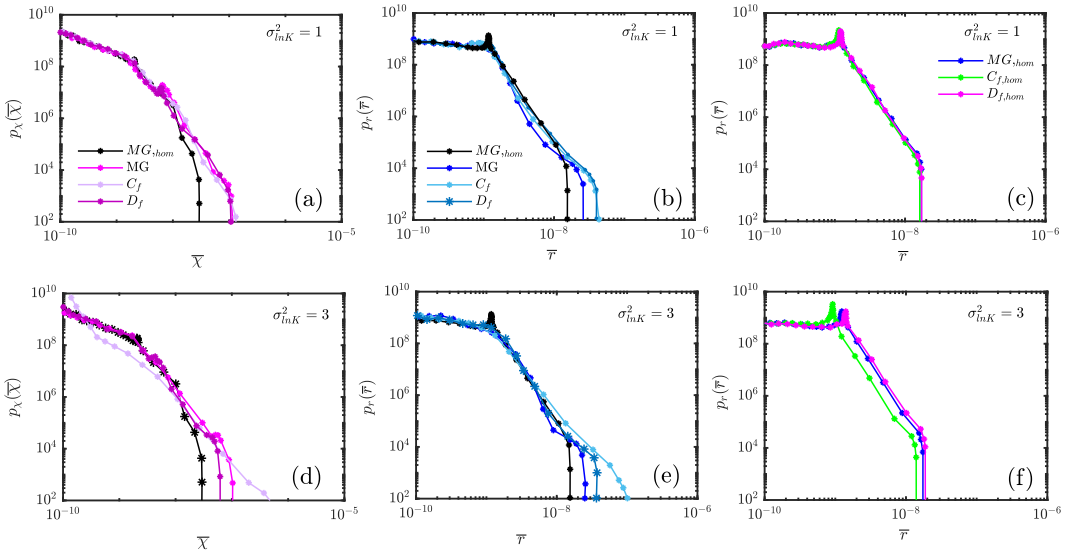

Figure C.5. PDF of the effective local mixing and reaction rates for the homogeneous field, the multi-Gaussian field (MG_{eff}), the connected field ($C_{f,eff}$) and the disconnected field ($D_{f,eff}$) for variances a-b) $\sigma^2_{lnK} = 1$ and c-d) $\sigma^2_{lnK} = 3$.

3 with a K_g of 5e-4 m/s. Note that we still idealise all layers as the same carbonate sequence, only with different hydraulic conductivities.

Two additional scenarios were simulated in order to isolate the behaviour of reaction and mixing for a stratified case where a single layer is sandwiched by two aquifers of the same hydraulic conductivity. In the first case, we have a low-high-low ($K_1 : K_2 : K_1$) scenario, where K_1 has a hydraulic conductivity of 5e-4 m/s and K_2 has an a hydraulic conductivity of 5e-3 m/s. In the high-low-high ($K_2 : K_1 : K_2$) scenario, K_1 has a hydraulic conductivity of 1e-3 m/s and K_2 has a hydraulic conductivity of 1e-4 m/s. The width of the middle layer in both cases is 20 m.

C.6 Flow deformation

The deformation of the field largely controls the presence of enhanced mixing and reactions. The deformation rate tensor is defined by

$$\boldsymbol{\epsilon}(\mathbf{x}) = \begin{pmatrix} \frac{\partial v_x(\mathbf{x})}{\partial x} & \frac{\partial v_x(\mathbf{x})}{\partial z} \\ \frac{\partial v_z(\mathbf{x})}{\partial x} & \frac{\partial v_z(\mathbf{x})}{\partial z} \end{pmatrix} \tag{C.12}$$

The strain tensor is given by $\boldsymbol{\Theta}(\mathbf{x})$

$$\boldsymbol{\Theta}(\mathbf{x}) = \frac{1}{2}\left[\boldsymbol{\Theta}(\mathbf{x}) + \boldsymbol{\Theta}(\mathbf{x})^\top\right], \tag{C.13}$$

where the superscript $\top$ denotes the transpose. The strain rate $\sigma(\mathbf{x})$ is defined as the determinant of the strain tensor,

$$\sigma(\mathbf{x}) = \epsilon_{11}^2 + (\epsilon_{12} + \epsilon_{21})^2. \tag{C.14}$$

It is a measure for the local stretching of a fluid element.

References

Abarca, E. (2006), Seawater intrusion through heterogeneous aquifers, Ph.D. thesis, Universitat Politècnica de Catalunya.

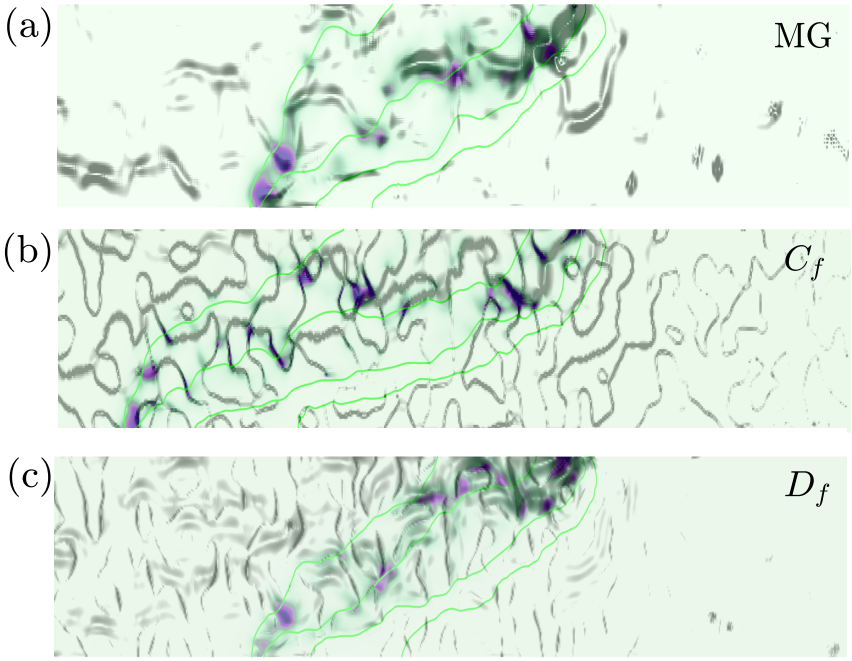

Figure C.6. Example of reaction rate maps overlying the diistribution of strain rates for σ^2_{lnK} = 3 for a) multi-Gaussian field (MG), (b) the connected field (C_f) and (c), the disconnected field (D_f).

Audra, P., and A. Palmer (2015), Research frontiers in speleogenesis . Dominant processes , hydrogeological conditions and resulting cave patterns, *Acta Carsologica*, *44*(3), 315–348, doi:10.3986/ac.v44i3.1960.

Back, W., B. B. Hanshaw, T. E. Pyle, L. N. Plummer, and A. E. Weidie (1979), Geochemical significance of groundwater discharge and carbonate solution to the formation of Caleta Xel Ha, Quintana Roo, Mexico, *Water Resources Research*, *15*(6), 1521–1535, doi:10.1029/WR015i006p01521.

Back, W., B. B. Hanshaw, U. S. G. Survey, J. S. Herman, E. Sciences, J. N. V. Driel, and U. S. G. Survey (1986), Differential dissolution of a Pleistocene reef in the ground-water mixing zone of coastal Yucatan , Mexico, *Geology*, *14*(February), 137–140.

Bear, J. (1988), *Dynamics of fluids in porous media.*, Dover publications, inc New York.

Dagan, G. (1987), Theory of solute transport by groundwater, *Annu. Rev. Fluid Mech.*, *19*(1), 183–213, doi:10.1146/annurev.fluid.19.1.183.

De Simoni, M., J. Carrera, and M. W. Saaltink (2007), A mixing ratios-based formulation for multicomponent reactive transport, *Water Resources Research*, *43*, 1–10, doi:10.1029/2006WR005256.

Dentz, M., T. Le, A. Englert, and B. Bijeljic (2011), Mixing , spreading and reaction in heterogeneous media : A brief review, *Journal of Contaminant Hydrology*, *120-121*, 1–17, doi:10.1016/j.jconhyd.2010.05.002.

Filipponi, M., P.-y. Jeannin, and L. Tacher (2009), Geomorphology Evidence of inception horizons in karst conduit networks, *Geomorphology*, *106*(1-2), 86–99, doi:10.1016/j.geomorph.2008.09.010.

Gabrov, F., P. Häuselmann, and P. Audra (2014), Looping caves' versus water table caves': The role of base-level changes and recharge variations in cave development, *Geomorphology*, *204*, 683–691, doi:10.1016/j.geomorph.2013.09.016.

Gelhar, L. W. . (1993), *Stochastic subsurface hydrology*, Prentice-Hall.

Gelhar, L. W. (2003), *Applied Stochastic Hydrogeology*, Oxford University Press.

Groves, C. G., and A. Howard (1994), Early development of karst systems . I . Preferential flow path enlargement under laminar flow, *Water Resour. Res*, *30*(October), 2837–2846, doi:10.1029/94WR01303.

Held, R, S.Attinger, W. (2005), Homogenization and effective parameters for the Henry problem in heterogeneous formations, *Water Resources Research*, *41*, 1–14, doi:10.1029/2004WR003674.

Hidalgo, J. J., and M. Dentz (2018), Mixing across fluid interfaces compressed by convective flow in porous media, *Journal of Fluid Mechanics*, pp. 105–128, doi: 10.1017/jfm.2017.888.

Jouves, J., J. Jouves, S. Viseur, B. Ar, C. Baudement, and H. Camus (2017), Speleogenesis , geometry , and topology of caves : A quantitative study of 3D karst conduits Geomorphology Speleogenesis , geometry , and topology of caves : A quantitative study of 3D karst conduits, *Geomorp*, *298*(January), 86–106, doi: 10.1016/j.geomorph.2017.09.019.

Kerrou, J., and P. Renard (2010), A numerical analysis of dimensionality and heterogeneity effects on advective dispersive seawater intrusion processes, *Hydrogeology Journal*, *18*(1), 55–72, doi:10.1007/s10040-009-0533-0.

Lowe, D. J. (1992), The origin of limestone caverns : an inception horizon hypothesis, Ph.D. thesis, Manchester Polytechnic.

Michael, H. A., K. C. Scott, M. Koneshloo, X. Yu, M. R. Khan, and K. Li (2016), Geologic influence on groundwater salinity drives large seawater circulation through the continental shelf, *Geophysical Research Letters*, pp. 782–791, doi: 10.1002/2016GL070863.Received.

Mylroie, J. E., and J. L. Carew (1990), Mylroie, J. E., & Carew, J. L. (1990). The flank margin model for dissolution cave development in carbonate platforms. Earth Surface Processes and Landforms, 15(5), 413424. doi:10.1002/esp.3290150505, *Earth Surface Processes and Landforms*, *15*, 413–424.

Ng, K. C., and B. Jones (1995), Hydrogeochemistry of Grand Cayman, British West Indies: implications for carbonate diagenetic studies, *Journal of Hydrology*, *164*(1-4), 193–216, doi:10.1016/0022-1694(94)02556-Q.

Palmer, A. (1992), Origin and morphology of limestone caves, *Geological Society of America Bulletin*, *103*(January 1991), 1–21.

Parkhurst, D. L., and C. Appelo (2013), Description of input and examples for PHREEQC version 3–A computer program for speciation, batch-reaction, one-dimensional transport, and inverse geochemical calculations, chap. A43, p. 497, U.S. Geological Survey.

Pool, M., V. E. A. Post, and C. T. Simmons (2015), Effects of tidal fluctuations and spatial heterogeneity on mixing and spreading in spatially heterogeneous coastal aquifers, pp. 1570–1585, doi:10.1002/2014WR016068.Received.

Ranz, W. E. (1979), Applications of a Stretch Model to Mixing , Diffusion , and Reaction in Laminar and Turbulent Flows, *The American Institute of Chemical Engineers*, *25*(1), 41–47.

Renard, P., and G. de Marsily (1997), Calculating equivalent permeability: A review, *Adv. Water Resour.*, *20*(5-6), 253–278.

Rezaei, M., E. Sanz, E. Raeisi, and C. Ayora (2005), Reactive transport modeling of calcite dissolution in the fresh-salt water mixing zone, *Journal of Hydrology*, *311*, 282–298, doi:10.1016/j.jhydrol.2004.12.017.

R.K. Stoessell, W.C. Ward, B.H. Ford, J. S. (1989), Water Chemistry and CaCO3 dissolution in the saline part of an open flow mixing zone, coastal Yucatan Peninsula, Mexico, *Geological Society of America Bulletin*, *101*, 159–169.

Sanchez-Vila, X., A. Guadagnini, and J. Carrera (2006), Representative hydraulic conductivities in saturated groundwater flow, *Rev. Geophys.*, *44*, RG3002.

Sanford, W. E., and L. F. Konikow (1989), Simulation of Calcite Dissolution and Porosity Changes in Saltwater Mixing Zones in Coastal Aquifers, *Water Resources Research*, *25*(4), 655–667.

Sebben, M. L., A. D. Werner, and T. Graf (2015), Seawater intrusion in fractured coastal aquifers: A preliminary numerical investigation using a fractured Henry problem, *Advances in Water Resources*, *85*, 93–108, doi:10.1016/j.advwatres.2015.09.013.

Smart, P. L., J. M. Dawans, and F. Whitaker (1988), Carbonate dissolution in a modern mixing zone, *Nature*, *335*(6193), 811–813, doi:10.1038/335811a0.

Voss, C. I., and A. Provost (2002), A model for saturated-unsaturated variable-density ground-water flow with solute or energy transport, *Tech. rep.*

Zinn, B., and C. F. Harvey (2003), When good statistical models of aquifer heterogeneity go bad: A comparison of flow, dispersion, and mass transfer in connected and multivariate Gaussian hydraulic conductivity fields, *Water Resources Research*, *39*(3), 1–19, doi:10.1029/2001WR001146.